β-$SrZrS_3$: A superior intermediate temperature thermoelectric through complex band geometry and ultralow lattice thermal conductivity

Surbhi Ramawat, Sumit Kukreti, and Ambesh Dixit*
Advanced Materials and Device (A-MAD) Laboratory, Department of Physics, Indian Institute of Technology, Jodhpur 342030, India

(Received 6 May 2023; revised 17 July 2023; accepted 28 July 2023; published 18 August 2023)

The pursuit of high-performance thermoelectricity has generated an endless stream of suitable materials, but those having intrinsically low thermal conductivity are highly desirable for production. Here, we demonstrated intrinsically low lattice thermal conductivity (κ_l) for the orthorhombic phase β-$SrZrS_3$, a chalcogenide perovskite. The weak interatomic interactions are noticed for SrS_8 bicapped trigonal prism geometry, leading to the bond heterogeneity and thus an effective anharmonicity in the system. This anharmonicity facilitates the low κ_l. The average κ_l value at 300 K is found to be $\sim$1.26 W m^{-1} K^{-1}, while at 800 K it further reduces to a lower value of $\sim$0.48 W m^{-1} K^{-1} due to enhanced phonon-phonon scattering. The presence of several valleys within a small energy offset from the primary conduction-band edge and a sort of pudding-mold-kind appearance make the band structure more complex. These band features in the conduction band facilitate the system with a high-power factor with n-type doping. Avoiding bipolar conduction is also confirmed via a large-band-gap value of $\sim$2.04 eV for β-$SrZrS_3$. Furthermore, significant phonon-phonon scattering is caused by the high anharmonic interaction resulting from the coupling of the acoustic and low optical frequency domains, substantiating the low κ_l. Additionally, the electron's lifetime at 300 K is $\sim$34 fs and its mobility is $\sim 10^2$ cm^2 V^{-1} s^{-1}. Thus, an impressive figure of merit >2 is achieved for the intermediate temperature (600–800 K) at an experimentally feasible electron doping of $\sim 10^{20}$ cm^{-3}, indicating that β-$SrZrS_3$ could be an excellent wide-band-gap thermoelectric material.

DOI: 10.1103/PhysRevMaterials.7.085403

I. INTRODUCTION

With its potential to harness green energy via directly converting heat to electricity, the technology of thermoelectricity has been shown to be a contemporary alternative to the power industry [1–6]. Along with their widespread space-based applications and solar thermoelectric generators, thermoelectric (TE) devices are also being used in cutting-edge technologies such as industrial waste heat recovery, medical devices, microscale cooling, etc. [7–10]. However, commercial application has long been limited due to the low efficiency of the available materials. Research and development efforts toward designing new materials in the past few decades have led to a new surge of interest in the global market. At a certain operating temperature, the performance of TE material is usually quantified with a dimensionless figure of merit $ZT = \sigma S^2 T/(\kappa_e + \kappa_l)$, where σ, S, and T are the electrical conductivity, the Seebeck coefficient, and the absolute temperature, respectively, and κ_e and κ_l are the carrier thermal conductivity and the lattice thermal conductivity, respectively. A good TE material is considered to have $ZT \geqslant 1$ and possess a high power factor (PF $= S^2\sigma$) with low thermal conductivity [11–13]. Band-engineering methods [14] may be used to enhance the electrical component, such as the power factor (PF), but they are not straightforward as σ, S, and κ_e are all interdependent parameters, and κ_e could be related to σ as given by the Wiedemann-Franz law $\kappa_e = L\sigma T$, where L is the Lorenz number, which varies with the doping level in semiconductors [15]. Therefore, it is challenging to enhance the PF while simultaneously reducing κ_e. However, κ_l is found to be relatively independent, therefore it seems appropriate to decrease κ_l by affecting phonon transport in order to attain a high ZT [16]. Several state-of-the-art methods, such as alloying, nanostructuring, and introducing anharmonicity by creating defects in the system, have also been employed to regulate κ_l extensively. However, finding TE compounds with intrinsically low κ_l is a challenging task, and it always takes top priority over tuning κ_l via different engineering [17,18].

In the past few decades, chalcogenides like PbTe, Bi_2Te_3, and their alloys have been established as commercially viable for high ZT value, due to their intrinsically low thermal conductivity and large PF at intermediate- and low-temperature ranges, respectively [19–21]. Materials such as PbS, GeTe, SnSe, SnTe, Sb_2Te_3, In_4Se_3, and BiCuSeO are also being regarded as promising thermoelectric systems for intermediate temperature (500–900 K) [22]. Unique bonding properties such as the metavalent bond between a metal and a chalcogen atom, which supports strong anharmonicity, make it possible for these materials to have intrinsically low lattice thermal conductivity [23,24]. In addition, the high carrier mobility in these compounds contributes to their superior thermoelectric performance. Moreover, several oxides such as $PbTiO_3$, $BaTiO_3$, and $SrTiO_3$ are also being investigated due to the feasibility of doping and higher chemical stability in the oxidizing environment, but they are often limited by large κ_l and

*ambesh@iitj.ac.in

low carrier mobility [25,26]. Therefore, material exploration for thermoelectricity within the chalcogenide family, but with nontoxic constituents, is of the utmost importance today in order to compete with conventional materials [9,27].

Following chalcogenides, a new family belonging to perovskites, namely chalcogenide perovskites (ABX_3, A, B = metals and X = S, Se), have recently attracted a great deal of attention among researchers. Instead of unconventional bonding, i.e., tuning electronic properties by controlling octahedral tilts, substituting A and B cation sites enables these ternary compositions with a larger design space than well-studied binary chalcogenides. Interestingly, the nontoxic composition-based chalcogenide perovskites also support environmentally friendly materialization of TE devices [28,29]. Numerous experimental and theoretical investigations have been carried out, showing the successful formation of chalcogenide perovskites with promising applications [30–32]. For example, $CaTiS_3$, $BaZrS_3$, $CaZrSe_3$, and $CaHfSe_3$, with their distorted perovskite structure and high optical absorption yielding a tunable band gap ranging from 1 to 1.8 eV, are found to be applicable for photovoltaics [33]. Perera *et al.* [34] successfully synthesized the broad family of ABS_3 (A = Ca, Sr, Ba; B = Zr, Ti) using high-temperature sulphurization of the oxide with CS_2, and the band gap was reported within the 1.73–2.87 eV range. A few reports based on first-principles computation recently presented Zr-based chalcogenides—$CaZrS_3$, $CaZrSe_3$, and $BaZrS_3$—as potential thermoelectric materials exhibiting ultralow lattice thermal conductivity and a large Seebeck coefficient [35,36]. In another study of 40 promising materials of the same family, it was revealed that on the one hand, the much softer interatomic bonding interactions compared to their oxide counterparts provide strong anharmonicity, while on the other hand, the combination of a pudding-mold-type band structure with high valley degeneracy renders a high PF > 4 [37].

Our choice of material is motivated by the fact that $SrZrS_3$ is one of the few ternary chalcogenides that has been experimentally synthesized in two structures modifications, namely needlelike α-$SrZrS_3$ and distorted perovskite-β-$SrZrS_3$ with band-gap values 1.53 and 2.13 eV, respectively [38]. α-$SrZrS_3$ is referred to as nonperovskite due to its edge-sharing ZrS_6 octahedra with low electronic dimensionality, while β-$SrZrS_3$ has a distorted perovskite structure with higher electronic dimensionality [39]. Usually, materials with low electron dimensionality are complex for device application because they should be grown with a special crystallographic orientation to facilitate effective carrier transport [40]. Therefore, unlike the α-phase, β-$SrZrS_3$ could be a suitable choice for photovoltaic, thermoelectric, and optoelectronic applications. In addition, the possibility of bond heterogeneity among Sr-S and Zr-S seems advantageous in terms of anharmonicity. To date, we have found no detailed study on using the band structure and atom bonding effect of β-$SrZrS_3$ chalcogen perovskite to predict thermoelectric metrics.

In this study, we present the thermal and electronic transport properties of β-$SrZrS_3$ using first-principles calculations with *ab initio* scattering and transport theory. Initially, structural analysis is carried out utilizing bond strength and mechanical properties, which indicates a soft covalent bond between the metal and sulfur along with a more ductile nature. Electronic analysis reveals a complex band structure comprising multiple valleys near the conduction-band edge, including a pudding-mold-type band feature, ultimately benefiting the thermoelectrics. Next, the three-phonon scattering mechanism is employed to understand the low lattice thermal conductivity, which also correlates with the system's strong anharmonicity. Further, in computing the carrier relaxation time by considering the elastic acoustic deformation potential scattering, the role of ionized impurity scattering and inelastic polar optical phonon scattering is examined. Finally, we demonstrate that β-$SrZrS_3$ is suitable for intermediate temperature thermoelectric application as ZT is ∼2.56 at 600 K and reaches ∼3.67 at 800 K for electron doping.

II. METHODS

All first-principles calculations are performed in the framework of density functional theory (DFT) using the Vienna Ab-initio Simulation Package (VASP) [40]. The Kohn-Sham equations are solved variationally in a plane-wave basis set with a high kinetic energy cutoff of 450 eV using the projected-augmented-wave (PAW) method [41]. The Perdew-Burke-Ernzerhof (PBE) exchange-correlational functional is adopted [42] for structural optimization by considering 10^{-10} eV and 10^{-3} eV/Å as the convergence criteria for energy and force, respectively. The Heyd-Scuseria-Ernzerhof (HSE06) [43] hybrid functional is used for a more reliable band gap, and the Brillouin zone is sampled using a $7 \times 5 \times 7$ k-point grid in the Gamma-scheme. Spin-orbit coupling (SOC) has not been considered because it does not alter the electronic structure, as shown in the Supplemental Material (Fig. S2) [44]. Using the LOBSTER code, the chemical bond analysis based on chemical orbital Hamilton population (COHP) is investigated [45].

Second-order (harmonic) interatomic force constants (IFCs) are computed by applying the finite displacement method on the $2 \times 2 \times 2$ supercell via PHONOPY [46]. Third-order (anharmonic) IFCs are extracted via third-order.py [47] using a real-space supercell approach combined with DFT calculations. The supercell's size and the interatomic interaction's cutoff are critical parameters while calculating the anharmonic IFCs. In principle, the interaction's cutoff should exceed the range of physically relevant interactions to get an accurate result [48]. However, to reduce computational cost, the convergence test is usually performed with the interaction cutoff for the considered supercell in order to avoid the possibility of under- or overestimating the calculated lattice thermal conductivity [49]. Here we employed the same $2 \times 2 \times 2$ supercell size and found the converged interaction cutoff as tenth nearest neighbors for the fitting to obtain the third-order IFCs (see Fig. S3 in the Supplemental Material [44]).

The lattice thermal conductivity at temperature T can be explained by [47]

$$k_l^{\alpha\beta} = \frac{\hbar^2}{k_B T^2 N \Omega} \sum_{\lambda} f_0(f_0+1)(\omega_\lambda)^2 v_\lambda^\alpha v_\lambda^\beta \tau_\lambda, \qquad (1)$$

where α and β represent the Cartesian axes, and Ω, N, and f_0 are the volume of the unit cell, the number of k-points,

and Bose-Einstein statistics, respectively. Further, ω_λ denotes the angular frequency of the phonon mode, v_λ^α and v_λ^β are the group velocity components, and τ_λ is the self-consistent phonon lifetime. The extracted second- and third-order IFCs are encoded in SHENGBTE [47] to get lattice thermal conductivity (κ_l) and phonon scattering rates. A converged q-point sampling of a $15 \times 15 \times 15$ grid with scalebroad parameter 0.1 is adopted to solve phonon Boltzmann transport equations. The Supplemental Material covers more information on the q-point and scalebroad convergence test [44].

The electronic transport coefficients are calculated by *ab initio* scattering and the transport method implemented in the AMSET code [50], which solves the electronic Boltzmann transport equation in the momentum relaxation-time approximation (MRTA) to calculate scattering rates and mobilities within the Born approximation. In the AMSET code, the relaxation time is estimated by the number of different band and k-point dependent scattering approaches instead of the constant relaxation-time approach. In this work, we calculated scattering rates by considering the following: (a) acoustic deformation potential (ADP), which is responsible for the phonon-electron interactions; (b) ionized impurity (IMP) scattering, which represents scattering of charge carriers by ionization of the lattice; and (c) polar optical phonon (POP) scattering, which considers the interaction between polar optical phonons and electrons. The resulting carrier relaxation time, the inverse of the scattering rate, can be calculated by Matthiessen's rule:

$$\frac{1}{\tau} = \frac{1}{\tau^{\mathrm{ADP}}} + \frac{1}{\tau^{\mathrm{IMP}}} + \frac{1}{\tau^{\mathrm{POP}}}, \tag{2}$$

where τ^{ADP}, τ^{IMP}, and τ^{POP} are the relaxation times from the ADP, IMP, and POP scattering, respectively. In ADP and IMP scatterings, electrons do not acquire or lose energy showing elastic scattering, whereas POP scatterings exhibit inelastic scattering that occurs due to phonon emission or absorption. The Fermi golden rule used to calculate the scattering rates for elastic and inelastic scattering from an initial nk state to a final $mk + q$ state can be written as follows [50]:

$$\tau^{-1}_{nk\to mk+q} = \frac{2\Pi}{\hbar}|g_{nm}(\boldsymbol{k},\boldsymbol{q})|^2\delta(\varepsilon_{nk} - \varepsilon_{mk+q}), \tag{3}$$

$$\tau^{-1}_{nk\to mk+q} = \frac{2\Pi}{\hbar}|g_{nm}(\boldsymbol{k},\boldsymbol{q})|^2\left[\left(n_q + 1 - f^0_{mk+q}\right)\delta\left(\Delta\varepsilon^{nn}_{k,q} - \hbar\omega_q\right) + \left(n_q + f^0_{mk+q}\right)\delta\left(\Delta\varepsilon^{nm}_{k,q} + \hbar\omega_q\right)\right], \tag{4}$$

where $\hbar$, δ, n, and f are the Planck's constant, a Dirac delta function, Bose-Einstein distribution, and Fermi-Dirac distribution. ε_{nk} corresponds to the energy of the $|nk\rangle$ state, and $g_{nm}(\boldsymbol{k},\boldsymbol{q})$ is the coupling matrix element of the considered scattering mechanism. Detailed forms of all the scattering matrix elements are discussed in [50]. The $-\hbar\omega_q$ and $+\hbar\omega_q$ correspond to the photon emission and absorption. The required parameters to obtain the scattering rates, such as dense and uniform band structures, elastic coefficients, wave-function coefficients, deformation potentials, static and high-frequency dielectric constants, and polar-phonon frequency, are calculated by the DFT and density functional perturbation theory (DFPT) given in the Supplemental Material [44]. An interpolation factor of 200 is used with the $79 \times 57 \times 83$ dense k-grid to predict carrier relaxation time and carrier mobility. Further, the Seebeck coefficient, electrical conductivity, and electronic thermal conductivity were calculated using the BOLTZTRAP2 code [51], with reliable carrier relaxation time obtained from the AMSET code.

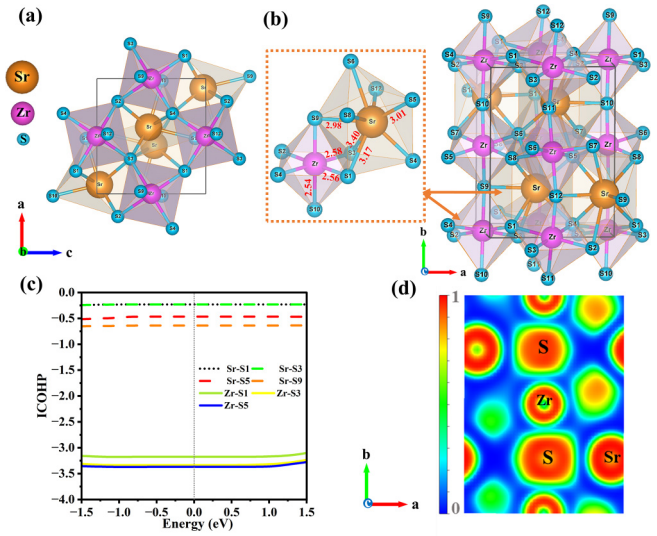

FIG. 1. The crystal structure of orthorhombic distorted perovskite β-$SrZrS_3$. (a) Top and (b) front view along with the zoom-in of the corner shared octahedra ZrS_6 and bicapped trigonal prism geometry SrS_8 with the Zr-S and Sr-S bond lengths marked. VESTA software is used for visualization [53]. Regarding bond lengths, Zr-S1, Zr-S3, and Zr-S10 bonds are equivalent to the Zr-S2, Zr-S4, and Zr-S9 bonds. Similarly, Sr-S1, Sr-S3, Sr-S5, and Sr-S9 bonds are equivalent to Sr-S8, Sr-S6, Sr-S4, and Sr-S12. (c) Integrated chemical orbital Hamiltonian population (ICOHP) of the Sr-S and Zr-S bonds up to the Fermi level. (d) The electronic localization function (ELF) along the (001) plane. ELF = 0 and 1.0 correspond to blue and red, denoting no electron and full electron localization, respectively.

III. RESULTS AND DISCUSSION

A. Structural properties

The optimized crystal structure of β-$SrZrS_3$, having space group *Pnma* (62), is presented in Fig. 1(a). It consists of 20 atoms in a unit cell. The lattice parameters for the unit cell containing four Sr, four Zr, and twelve S atoms are $a = 7.16$ Å, $b = 9.81$ Å, and $c = 6.77$ Å, agreeing well with the available experimental [52] and theoretical reports [39] (see Table I). Chalcogen perovskite β-$SrZrS_3$ exhibits a distorted orthorhombic perovskite structure. Here, Sr and Zr atoms have 2+ and 4+ cationic states. The Zr atoms are sixfold-coordinated to S atoms, forming a ZrS_6 distorted corner-sharing octahedron with a bond length in the range of 2.54–2.58 Å. In contrast, the alkaline earth element Sr shows eightfold coordination with S atoms in a bicapped trigonal prism geometry SrS_8, and a Zr-S bond length ranging from 2.99 to 3.40 Å [see Fig. 1(b)], signifying the noticeable heterogeneity in bond lengths that is the main source of anharmonicity in this system.

TABLE I. Calculated lattice constants and experiment values in bracket [52], Y, B, and G (in GPa), Pugh ratio (B/G), and Poisson ratio (υ).

β-$SrZrS_3$	a (Å)	b (Å)	c (Å)	Y	B	G	B/G	υ
Our calc. (expt.)	7.16 (7.10)	9.81 (9.75)	6.77 (6.73)	93.09	69.921	36.421	1.92	0.28

Generally, the sulfide and selenium chalcogenide [$AB(S/Se)_3$] perovskite's covalent character is more pronounced than their oxide-equivalent systems. This is due to the relatively lower electronegativity of S/Se atoms than oxygen atom. Further, we tried to quantify the nature of the bond by investigating the degree of covalency using Bader's electron density analysis. This method is used to enumerate the partial charge transfer between cations and anions; less charge transfer implies less ionic but more covalent hybridization between the atoms. Table S1 of the Supplemental Material [44] lists the computed Bader's charge on the constituent atoms of β-$SrZrS_3$. It signifies a comparatively smaller charge transfer in the Zr-S bond (∼50%) than the Sr-S bond (∼75%), providing the former bond with a more covalent character. Here, it is noteworthy that the various bond characters present in the system may generate an anharmonicity. Further, to measure the bond strength and possible anharmonicity in the compound, we also evaluated ICOHP (integration of COHP) near the Fermi energy, which is generally used to quantify the strength of all possible bonds in the system. In Fig. 1(c), we see that the ICOHP values for Sr-S interactions are in the range −0.25 to −0.74, while for Zr-S interaction the ICOHP value remains near −3.5, implying weaker bond strength between Sr and nearest-neighbor S atoms. It is also consistent with the decreasing order of bond lengths, as Zr-S bond lengths are shorter than Sr-S bond lengths.

Meanwhile, the bonding characteristics are also explored by the electron localization function (ELF) of the (001) plane evaluated by the following equation: $\mathrm{ELF}(r) = 1/1 + [D(r)/D_h(r)]^2$ [54], where $D(r)$ and $D_h(r)$ correspond to the Pauli kinetic energy density at a given point in real space r and homogeneous electron gas with the same density, respectively. The ELF values 0, 0.5, and 1 represent electron depletion, the behavior of homogeneous electron gas, and fully localized electrons, respectively. For β-$SrZrS_3$, Fig. 1(d) shows that the electrons are localized around Sr and S atoms, with an ELF value below 0.2 at the center of the shortest Sr-S bond, indicating ionic-like bonding for the same bond. On the other hand, a relatively larger ELF value of ∼0.4 is noticed between Zr and S atoms. This is an indication of good atomic interaction within the ZrS_6 octahedra providing a covalent-like nature with relatively more electron sharing in this unit. Overall, the ELF reflects that the bonding interactions steadily deteriorate in the following order: Zr-S > Sr-S bonds, which agrees with the Bader charge analysis. Consequently, because of the bond heterogeneity, as was also observed for the softer chemical bonds formed in SrS_8 bicapped trigonal prism geometry compared to ZrS_6 octahedra, the system acquires an ultimate phonon anharmonicity that significantly impacts the phonon contribution and determines a lower k_l value for β-$SrZrS_3$.

The strength of the chemical bonding with the order of flexibility is also reflected through the mechanical properties as more stiffness (i.e., higher sound velocity) in the crystal signifies high resistance to elastic deformation [55]. The weak bonding stiffness causes softening of the phonon modes, thus slowing down phonon propagation. Because of the orthorhombic symmetry of β-$SrZrS_3$, nine independent elastic constants C_{ij} are calculated, and an additional elastic modulus is derived, as listed in Table S2 in the Supplemental Material [44] (also see [56]). These elastic modulus values satisfy the Born-Huang mechanical stability criteria [56]. The bulk modulus (B) and Young's modulus (Y) give the material's compressibility and stiffness; larger values show larger compressibility and stiffness. B and Y values for β-$SrZrS_3$ are 69.92 and 93.09 GPa, which are close to the $BaZrS_3$ results of 69.9 and 86.6 GPa [57]. The shear modulus (G) is ∼36.42, which actually indicates shape resistance. The large B/G ratio >1.75 signifies the ductile behavior of the system as per the Pugh criteria, which is beneficial for developing flexible thermoelectric modules. Furthermore, the chemical bonding of the solid material is also evaluated by Poisson's ratio, i.e., $\upsilon < 0.2$ for covalent material, $0.2 < \upsilon < 0.3$ for ionic-covalent material, and $0.3 < \upsilon < 0.4$ for ionic material. Thus, β-$SrZrS_3$ is shown to be ionic-covalent material, which is quite consistent with the ELF analysis.

B. Electronic properties

The thermoelectric (TE) properties depend heavily on the accuracy of the band gap and the electronic states near the band edges. Figures 2(a) and 2(b) represent the computed band structure and density of states (DOS) of β-$SrZrS_3$, respectively. We see that both the valence-band maxima (VBM) and the conduction-band minima (CBM) are located at the Γ point, signifying direct band-gap character. Further, using the HSE06 functional, the calculated band gap is 2.04 eV, which is comparable with previous reports (see Table II). Importantly, this large band gap for β-$SrZrS_3$ is sufficient to avoid bipolar conduction [58], so the electronic transport properties would not be adversely affected. In addition, the conduction band, comprised of the hybridization of Zr-d and Sr-s states, exhibits multiple valleys with energies closer to the CBM. It is usually helpful for high-temperature thermoelectrics to have these extra bands with small energy offset (Δ) from the main conducting bands [59,60]. In β-$SrZrS_3$, instead of the primary CB edge, which is made up of the convergence of doubly degenerate parabolic bands at the Γ point, another parabolic band at the U point appears to make a secondary conduction-band edge with an offset energy $\Delta E = 47$ meV. Another valley is noticed at the Y point in the Brillouin zone, which is roughly 180 meV from the CBM. More interestingly, a somewhat flat band connection between the Γ and U valley, as seen in the band structure, imparts a pudding-mold-type of geometry to the conduction. The isoenergy Fermi surface, as shown in Fig. S1 of the Supplemental Material [44], for

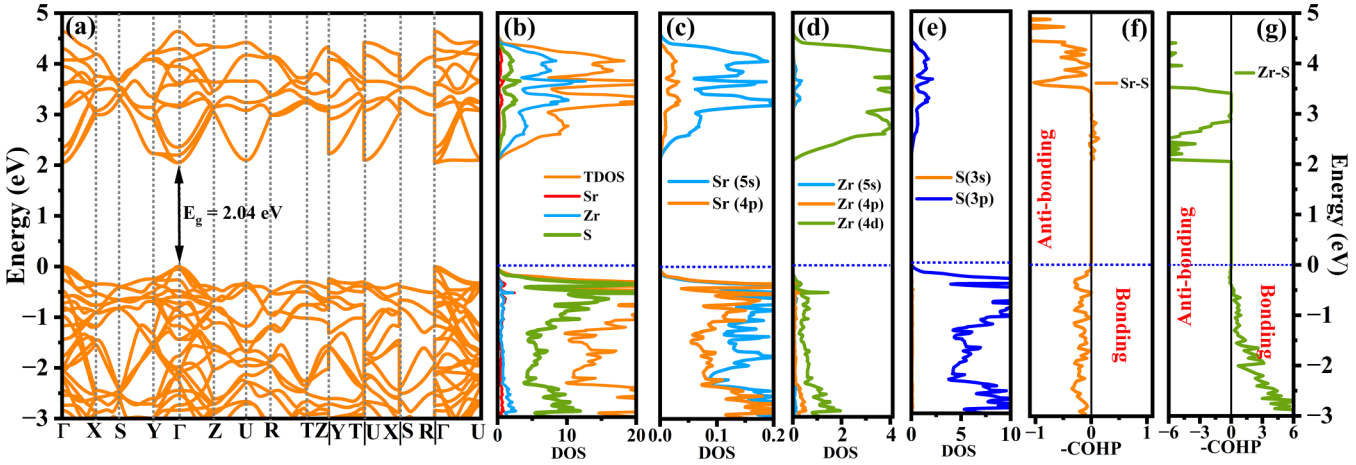

FIG. 2. (a) Electronic band structure of the β-$SrZrS_3$ calculated with the HSE06. (b) Atomic contribution of Sr, Zr, and S atoms along with total density of states. The different orbital contribution for Sr (c), Zr (d), and S (e) atoms on electronic density of states. [(f), (g)] Negative crystal orbital Hamiltonian population (-COHP) for Sr-S and Zr-S interaction in β-$SrZrS_3$. The bonding and antibonding interactions are shown by –COHP spikes on the right and left. The Fermi level is set to 0 eV and is shown with a blue dotted line.

an energy level above 47 meV from the primary conduction-band edge, also confirms the same. The pudding-mold-type band structure, which is dispersive in one direction and flat in the other, results in a high-power factor due to a large Seebeck coefficient and a larger Fermi surface, providing large conductivity with suitable carrier doping [61]. Unlike the complex band structure of the conduction band, we do not notice many valleys of small ΔE near the VBM, and the nearest valley belongs to the Y point with $\Delta E = 244$ meV, which is quite far with respect to conduction-band valleys. Moreover, the multiple band convergence, which is observed at the Γ point, suggests the possibility of high electrical conductivity (for example, as $\sigma = \sigma_1 + \sigma_2$ for two bands 1 and 2) for the system. Generally, the density-of-states effective mass (m_d^*) is employed to analyze the vast majority of thermoelectric data as given by $m_d^* = N_v^{2/3} m_b^*$, where N_v includes orbital degeneracy, and m_b^* is the average effective mass of the degenerate valleys [62,63]. For a given carrier concentration, a high Seebeck coefficient can be either due to a large degeneracy, N_v, or a large m_b^*. The aforementioned complex band geometry with large orbital degeneracy near the conduction-band edges for β-$SrZrS_3$ leads to an enhanced density-of-states effective mass at suitable carrier doping. In addition, due to the dispersive nature of the conduction- and valence-band edges, a variety of carrier effective masses (m^*) with anisotropy along different directions is noticed. The effective masses of the electron (hole) along the Γ-X, Γ-Y, Γ-Z, Γ-U, U-Z, U-R, U-X, and Y-T directions in the Brillouin zone are calculated as fractions of m_0 and summarized in Table II. The higher effective mass along all directions in the valence band is due to the low curvature near the valence-band edge and is mostly contributed by S-p orbitals. In addition, we plotted the crystal orbital Hamiltonian population (COHP), where the positive value of COHP signifies antibonding, while the negative value indicates bonding interaction. The Sr-S and Zr-S orbitals form antibonding states in the conduction band, while Sr-S antibonding and Zr-S bonding states can be seen below the valence-band edge. The relatively low DOS intensity for Sr orbitals with the low COHP value of the Sr-S bond further indicates that the Sr atom is weakly bound to the crystal, which also accords well with the structural analysis described in the previous section.

C. Phonon characteristics and lattice thermal conductivity

To shed light on lattice thermal conductivity, it is necessary to explore the phonon-dispersion relations, phonon density of states, and phonon transport such as phonon group velocities, the Grüneisen parameter, and anharmonic scattering rates. Phonon-dispersion relations for β-$SrZrS_3$ are evaluated by solving the dynamical matrix, obtained from the second-order force constants along the directions X-Γ-Z-T-Y-Γ of the Brillouin zone, as shown in Fig. 3(a). Since there are 60 phonon modes ($3N$, where $N = 20$ is the number of atoms in the primitive unit cell) for each q-point, only the three lowest branches are acoustic modes while the remaining 57 are optical modes.

TABLE II. The computed band-gap (experimental) values and effective masses of electron and hole of β-$SrZrS_3$ at CBM and VBM (in m_0), where $m_0 = 9.1 \times 10^{-31}$ kg.

	Band gap (eV)			$m^*(m_0)$							
System	PBE	HSE	Carrier type	Γ-X	Γ-Y	Γ-Z	Γ-U	U-Z	U-R	U-X	Y-T
β-$SrZrS_3$	1.22	2.04 (2.05) [64]	electron	0.45	0.6	0.46	1.52	0.46	0.30	0.48	0.60
			hole	0.89	0.80	0.61	0.79	0.70	0.46	1.02	0.74

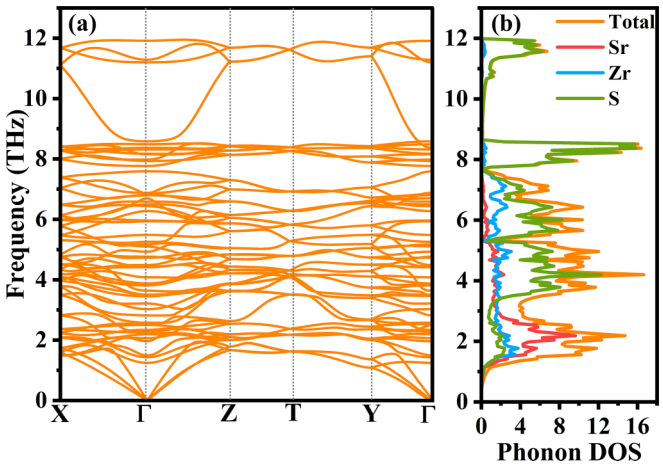

FIG. 3. (a) The calculated phonon-dispersion curve along the high-symmetry point in the Brillouin zone. (b) Phonon density of states with the orbital contribution.

All the positive frequencies in the dispersion curve indicate the dynamical stability of the orthorhombic β-$SrZrS_3$. The acoustic branches are found below a frequency of 1.81 THz. Notably, the low-lying optical modes (<2.46 THz) show strong hybridization with the longitudinal acoustic branches. The more or less flat geometry with the hybridized region would be suitable for large scattering channels and pave the way for low κ_l. In addition, a significant number of optical modes have moderate dispersion in the middle-frequency region, and a high dispersion is observed above 8.5 THz but with lower density. Therefore, the middle and high-frequency region is expected to have moderate and high group velocity, respectively, contributing some amount to the total lattice thermal conductivity, i.e., κ_l. The projected DOS suggests that the heavy elements Zr and Sr contribute most in the low-frequency region, while the contribution of the lighter element S is noticed effectively at the higher side of the frequency, as shown in Fig. 3(b). We observed a strong degeneracy between Sr and Zr in the acoustic and low optical region, which can be attributed to their similar elemental masses.

The Boltzmann transport equation is solved for a phonon with a self-consistent iterative method. We calculated lattice thermal conductivity as a function of temperature along the x-, y-, and z-axes as shown in Fig. 4(a). A decreasing trend in κ_l along with elevated temperature approximately follows the T^{-1} relation. This usually happens due to the inherent enhancement of phonon-phonon scattering at higher temperatures. For β-$SrZrS_3$, the κ_l values at 300 K are ~1.22, 1.26, and 1.31 $W\,m^{-1}\,K^{-1}$ along the x-, y-, and z-axes, respectively. Notably, the average κ_l value ~1.26 $W\,m^{-1}\,K^{-1}$ is significantly smaller than the extensively studied and

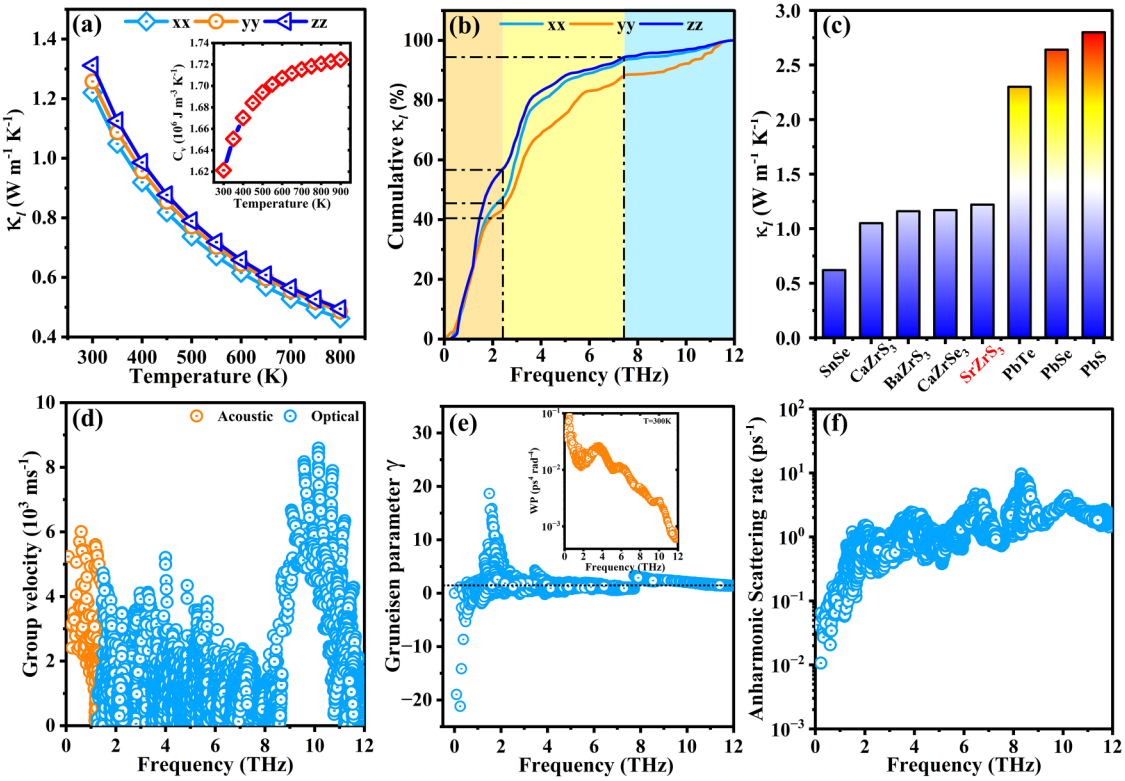

FIG. 4. (a) Lattice thermal conductivity as a function of temperature along the x-, y-, and z-axes. The inset shows specific heat as a function of temperature. (b) Cumulative lattice thermal conductivity (in %) at 300 K as a function of frequency. The orange, yellow, and blue represent the region of acoustic-lower optical mode, intermediate optical mode, and higher optical mode, respectively. (c) Comparison of lattice thermal conductivity at room temperature (300 K) with previously reported compounds, (d) phonon group velocity as a function of frequency with color-distinguished acoustic and optical modes, and (e) Grüneisen parameter as a function of frequency with the average shown by a dotted line. The inset shows a three-phonon scattering phase space at room temperature (300 K). (f) Anharmonic phonon scattering rate at 300 K.

well-known polycrystalline chalcogenides PbSe, PbTe [65], and oxide perovskites $PbTiO_3$, $BaTiO_3$ [25,26,66], and it is also found to be comparable to the chalcogenide perovskite reported in Refs. [35,36]; see Fig. 4(c). Further, for intermediate-temperature applications, it is desirable for TE materials to have ultralow κ_l. For β-$SrZrS_3$, we observe that the average κ_l approaches 0.64 and 0.48 $W\,m^{-1}\,K^{-1}$ at 600 and 800 K, respectively, indicating its suitability for intermediate-temperature TE generators. Additionally, as shown in the inset of Fig. 4(a), with increasing temperature the specific-heat value increases in the range of $(1.62–1.72) \times 10^6\,J\,m^{-3}\,K^{-1}$, which may provide a theoretical reference for experimentalists during the realization of TE devices.

The cumulative κ_l is another critical parameter that manifests in the contribution of phonons with different frequencies to the total κ_l. Similar to oxide perovskite, the value of κ_l for β-$SrZrS_3$ is determined largely by the optical modes as depicted in the normalized cumulative κ_l as a function of frequency at 300 K, as shown in Fig. 4(b) [67]. The data show that the acoustic and lower optical modes contribute ∼43%, 48%, and 57.2% along the x-, y-, and z-axes, respectively. At about 8.5 THz, a slight contribution to the total κ_l is observed, particularly along the y-direction, due to the lower density of phonon modes with rather significant dispersion in phonon spectra. However, above a frequency of 8 THz, the overall slope of the curve remains smaller and contributes ∼10%, confirming that the contribution of higher optical modes is relatively lower in total κ_l.

Understanding more about the low lattice thermal conductivity, we analyze the other critical parameters that affect the value of κ_l, such as frequency-dependent phonon group velocities, the Grüneisen parameter (γ), anharmonic scattering rates, and phase space (see Fig. 4). According to the kinetic theory, $\kappa_l = \frac{1}{3} C_v \bar{v}^2 \bar{\tau}$, where $\bar{v}$ and $\bar{\tau}$ are the average group velocities and relaxation time. We see that, in the acoustic region <1.81 THz, low-frequency phonons have a maximum group velocity (v_g) of up to 6000 $m\,s^{-1}$; see Fig. 4(d). The intermediate phonon modes, however, mostly have values up to 4000 $m\,s^{-1}$, while a larger $v_g \sim 8500\,m\,s^{-1}$ is noticed for some high-frequency optical modes. This is attributed to the extremely steeper phonon bands in these high-frequency regions, which signifies the non-negligible role of an optical phonon to the total κ_l, as phonons with larger v_g contribute effectively to thermal conduction.

Generally, the Grüneisen parameter "γ" characterizes the strength of the periodic crystal's anharmonicity and explains the change in phonon frequency concerning the change in unit-cell volume. According to Slack's theory, γ is inversely proportional to the square root of the lattice thermal conductivity (i.e., $\kappa_l \propto \frac{1}{\gamma^2}$) [68]. Indeed, the larger γ signifies strong anharmonicity and thus lower κ_l. As shown in Fig. 4(e), a jump in the value of γ near a frequency of 2 THz is observed for the acoustic and lower optical region signifying extreme anharmonic interaction, which further validates the strong coupling of these frequency modes in a narrow range. The computed average γ value is ∼1.46, which is comparable to that for PbSe (1.65), PbTe (1.69), and PbS (1.67) [65], signifying the reason behind the lower κ_l of β-$SrZrS_3$. Indeed, the soft metal-chalcogen covalent bond causes the strong anharmonicity that leads to low κ_l. Figure 4(f) shows the anharmonic phonon-phonon scattering rates as a function of frequency calculated at 300 K, which follows a similar trend to that of γ. Low anharmonic rates reflect the more significant lifetime of a phonon, and they would greatly increase κ_l, as seen from Fig. 4(f). The smallest values are below 1.8 THz frequency, which belongs to the acoustic region. Intermediate- and high-frequency optical phonon modes exhibit more scattering rates than acoustic modes. Enhanced coupling between lower frequency optical phonons facilitates more channels for scattering, resulting in a large, weighted phase space [see the inset of Fig. 4(e)], and it is attributed to the absence of an acoustic-optical phonon gap.

Consequently, significant scattering in the intermediate- and high-frequency regions, which is approximately one order more prominent than in the low-frequency region, plays a crucial role in deciding lower lattice thermal conductivity by contributing less to the total κ_l. Despite a high v_g value, the aforementioned strong coupling in acoustic and low optical branches, which results in larger scattering channels, is another source for lower κ_l; see Fig. 4(f). Overall, the large lattice anharmonicity and high scattering rates jointly contribute to the low lattice thermal conductivity for β-$SrZrS_3$.

D. Transport properties

We investigated the carrier relaxation time and the overall mobility by analyzing multiple scattering phenomena in the system (Fig. 5). These metrics are displayed for both hole (p-type) and electron (n-type) doping. As described in Sec. II, three essential carrier scattering rates (ADP, IMP, and POP) are considered in the present work. The overall and scattering-type resolved average relaxation time as a function of temperature at a fixed doping concentration $1 \times 10^{20}\,cm^{-3}$ are also investigated and shown in Figs. 5(a) and 5(d) for electron and hole doping, respectively. We noticed that the value of the electron (hole) lifetime decreases from 3.4×10^{-14} s (1.1×10^{-14} s) to 1.05×10^{-14} s (0.39×10^{-14} s) upon increasing the temperature from 300 to 800 K. In all temperature ranges, the ADP and IMP scattering-based lifetimes are about an order of magnitude larger than the POP lifetimes. However, the large POP scattering is found to reduce the total lifetime value. This can be further understood by analyzing all scatterings near the band edges, e.g., at 300 K shown in Figs. 5(b) and 5(e). The order of dominance for both conduction- and valence-band edges is POP > IMP > ADP. Usually, the POP scattering dominance is because of the pronounced polarity of the chemical bonds [69,70]. Instead, an overall increase in ADP scattering is noticed in the energy range close to the valence- and conduction-band edges, which typically happens due to the strong coupling between acoustic phonons and carriers. However, for the conduction band its values appear to stabilize a few meV above the edge, which may be due to the unchanged coupling of the acoustic phonon and electrons for a higher energy range. Furthermore, for the overall mobility for electrons (hole), the values are ∼110.5 (52.8) $cm^2\,V^{-1}\,s^{-1}$ and ∼31.3 (6.2) $cm^2\,V^{-1}\,s^{-1}$ at 300 and 800 K, respectively; see Figs. 5(c) and 5(f). The electrons' mobility is relatively higher than that of the holes, substantiating that for n-doping

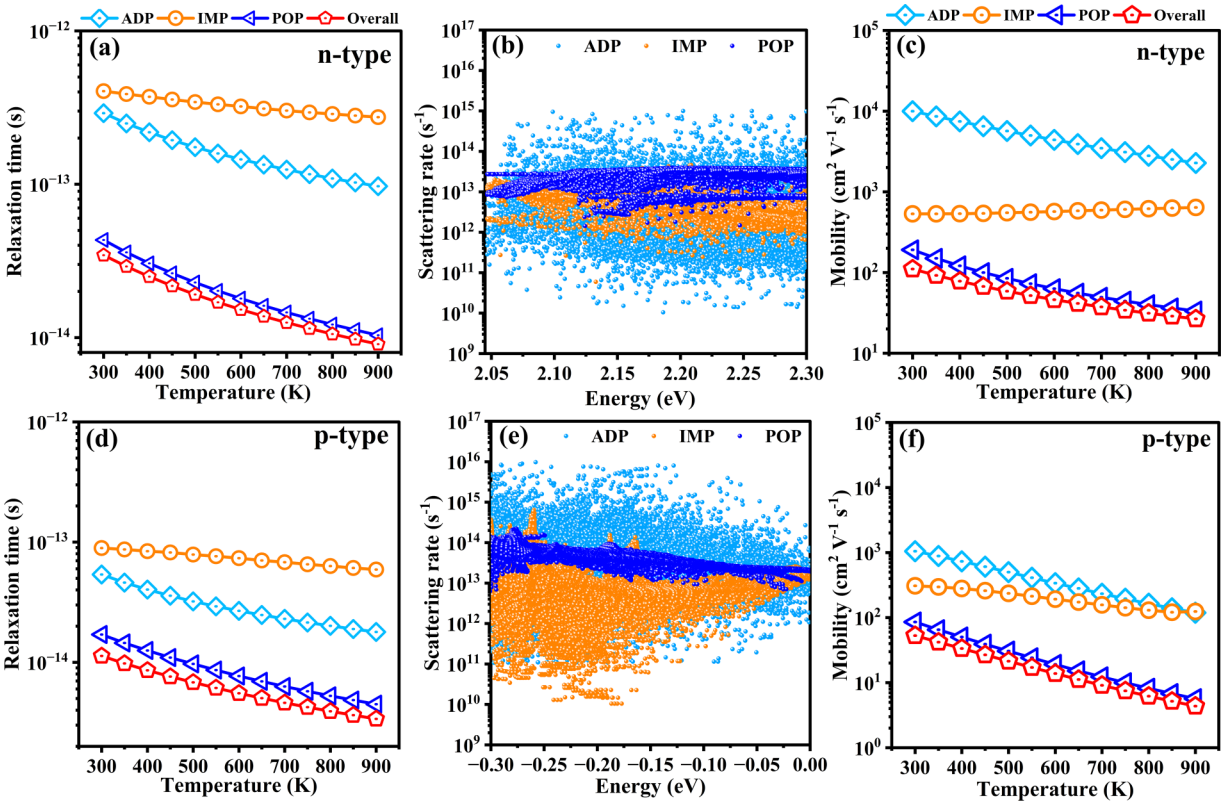

FIG. 5. [(a), (d)] The overall and scattering mechanism resolved the relaxation time for n-type and p-type doping. [(b), (e)] The ADP, IMP, and POP scattering rates contribution near the conduction- and valence-band edge as a function of energy at room temperature (300 K). [(c), (f)] The total and scattering mechanism resolved mobilities for n-type and p-type doping as a function of temperature. All the results have a doping concentration of 1×10^{20} cm^{-3}.

the material could essentially improve the TE figure of merit. Moreover, we note that ADP, POP, and the total mobilities decrease with increasing temperature, which can be attributed to the fact that the enhanced number of phonons contribute to high scattering. The scattering of IMPs is usually less impacted by temperature; therefore, their mobility remains rather consistent across the temperature range.

Figure 6 shows the calculated Seebeck coefficients, electrical conductivity, power factor, and electronic thermal conductivity with respect to carrier concentration at temperatures of 300, 600, and 800 K for both n-type and p-type doping along the x-, y-, and z-axes. Figures 6(a) and 6(e) show the calculated Seebeck coefficient of β-$SrZrS_3$ for both types of dopings. Note that the absolute values of "S" decrease with increasing carrier concentration and increase with increasing temperature, consistent with the formulas $S = \frac{8\pi^2 T}{3eh^2} \times (\frac{\pi}{3n})^{\frac{2}{3}} \times m_d^*$, where h, n, and m_d^* are Planck's constant, the carrier concentration, and the DOS effective mass near E_F, respectively. This implies that by adjusting the carrier concentration, one can also achieve a satisfactory value of S. For instance, at 1×10^{19} cm^{-3} carrier concentration, the value of $|S|$ for an electron (hole) is $\sim$354.6 (292.9) μV K^{-1} at 300 K and 466.5 (431.5) μV K^{-1} at 600 K along the x-direction, while in the y-direction it is 349.5 (268.2) μV K^{-1} at 300 K and 456.1 (394.8) μV K^{-1} at 600 K. We noticed that $|S|$ values for n-type are larger than that of p-type, indicating β-$SrZrS_3$ could be a good thermoelectric material with n-type doping. This large $|S|$ value, especially for n-type doping, could be correlated to multiple band degeneracy along with pudding-mold bands, which provides a significant density of state-effective mass. In addition, at 300 K, the slightly larger effective mass along the y-direction results in slightly larger $|S|$ along the y-direction than the x- and z-directions.

The electrical conductivity is directly dependent on carrier mobility as $\sigma = ne\mu$, where n, e, and μ are the carrier concentration, unit charge, and charge carrier mobility, respectively. Thus, following a similar trend for mobility, σ decreases with increasing temperature. However, an increase in carrier concentration also increases conductivity. For instance, along the x-direction, at $n = 1 \times 10^{19}$ cm^{-3}, σ_e (σ_h) is $\sim 3 \times 10^4$ (1.1×10^4) Sm^{-1}. At higher concentration, $n = 1 \times 10^{21}$ cm^{-3}, the σ_e (σ_h) is enhanced to 2.1×10^6 (6.6×10^5) S m^{-1} for 300 K. Further, monitoring Figs. 6(b) and 6(f), we see that σ shows almost similar values for electron doping along all the axes due to the more or less similar band dispersion along these directions with a similar number of converged bands. However, for hole doping, the σ value in the z-direction is lower, and this is because of the larger effective mass along this direction. Figures 6(c) and 6(g) show the electronic thermal conductivity as given by the Wiedemann-Franz law. κ_e is directly proportional to σ,

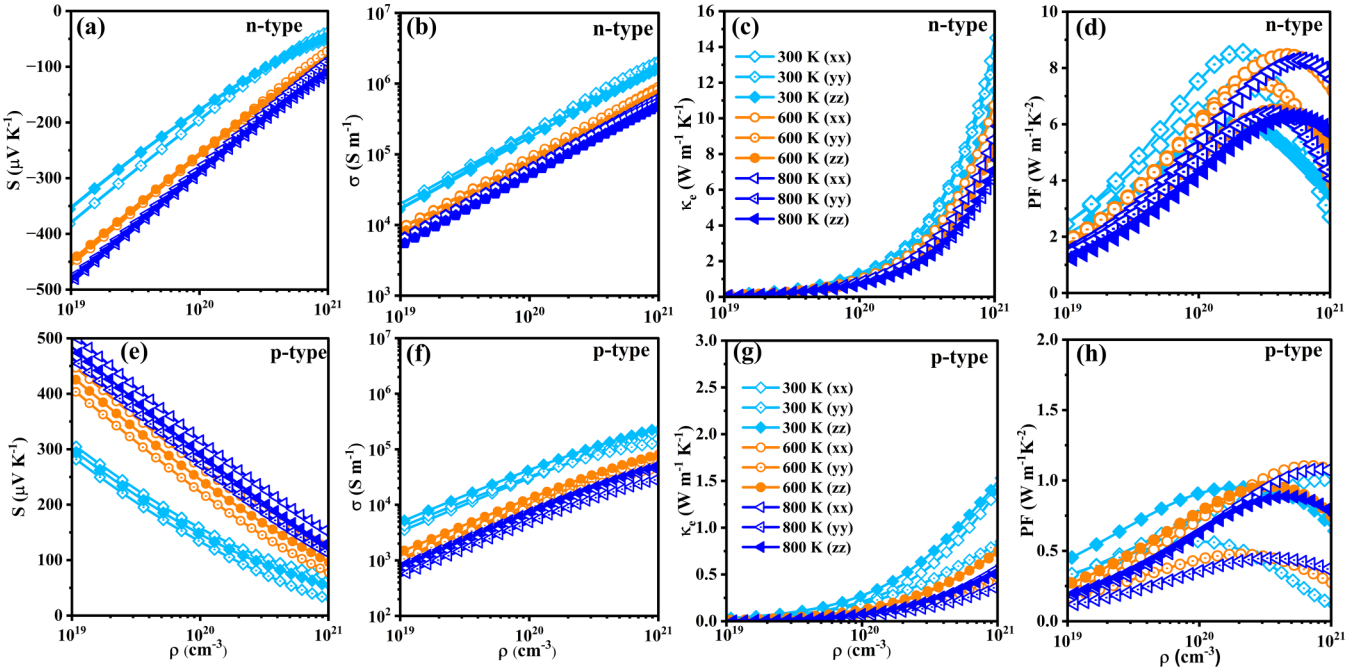

FIG. 6. The electronic transport properties as a function of carrier concentration with temperature 300, 600, and 800 K along the *x*-, *y*-, and *z*-axes. (a) Seebeck coefficient, (b) electrical conductivity, (c) electronic thermal conductivity, (d) power factor for *n*-type doping, (e) Seebeck coefficient, (f) electrical conductivity, (g) electronic thermal conductivity, and (h) power factor for *p*-type doping.

therefore the trend of κ_e is similar to that of σ, which increases with carrier concentration and decreases with temperature. κ_e can be ignored at the lower concentration regime until the carrier concentration approaches $1 \times 10^{20}\,\mathrm{cm}^{-3}$. Afterward, κ_e gradually increases with the carrier concentration and becomes comparable and even exceeds the lattice thermal conductivity κ_l, which is not desirable for the good TE performance of the materials. Further monitoring the trend along the *y*-direction, for example, the value of κ_e varies for the electron doping range 1×10^{19} to $1 \times 10^{20}\,\mathrm{cm}^{-3}$ from 0.20 to $1.71\,\mathrm{W\,m^{-1}\,K^{-1}}$ at 300 K, and for 600 K it increases from 0.11 to $1.09\,\mathrm{W\,m^{-1}\,K^{-1}}$. Similarly, for the hole doping range 1×10^{19} to $1 \times 10^{20}\,\mathrm{cm}^{-3}$, it varies from 0.02 to $0.26\,\mathrm{W\,m^{-1}\,K^{-1}}$ at 300 K, and for 600 K it changes from 0.01 to $0.12\,\mathrm{W\,m^{-1}\,K^{-1}}$. We see that for *n*-type doping, the κ_e values are always larger than the *p*-type doping when compared with the corresponding temperature and doping concentration, which are also correlated with the trend of σ. Furthermore, the power factor ($\mathrm{PF} = \mathrm{S}^2\sigma$) as a function of carrier concentration at various temperatures enables us to determine the optimal doping for the best possible thermoelectric output within the framework of electronic transport. Initially, the PF increases and then decreases with the carrier concentration; the opposite trend for *S* and σ leads to a high PF at moderate concentrations; see Figs. 6(d) and 6(h). Due to the anisotropic behavior of *S* and σ, the PF also follows the anisotropy among different axes at the same temperatures. Due to the large $|S|$ and σ value, a larger PF is noticed. For instance, at 600 K, for $5 \times 10^{20}\,\mathrm{cm}^{-3}$ *n*-type doping, its value is $\sim 8.5\,\mathrm{mW\,m^{-1}\,K^{-2}}$, while at the same *p*-type doping concentration, it is found to be $\sim 1.2\,\mathrm{mW\,m^{-1}\,K^{-2}}$. Here, we see a dramatic increase in the PF, which is consistent across all temperature ranges and results from the seemingly one-order increase in the σ value between *p*-type and *n*-type doping at 600 K. The appreciable *n*-type power factor for β-$SrZrS_3$ is attributed to the multivalley, degenerate band's convergence, with a pudding-mold-type band geometry, that together provide relatively large σ and *S* over a doping range.

E. Figure of merit

After a detailed investigation of the thermoelectric transport properties with the lattice thermal conductivity, we computed the average *ZT* for β-$SrZrS_3$ as a function of carrier concentration for different temperatures. The direction-oriented *ZT* for electron and hole doping exhibited anisotropy as depicted in Fig. 7. Since the *ZT* values for *n*-type doping are greater than those for *p*-type doping, the *n*-type doping can effectively enhance the TE performance of $SrZrS_3$. For example, at 300 K, the *ZT* value of *n*-type doping is 0.97, which is approximately six times that of 0.17 for *p*-type doping; see Figs. 7(a) and 7(b). Further, at 800 K the maximum *ZT* is achieved. For *n*-type (*p*-type) it is ~3.67 (1.10) at an optimal doping concentration $\sim 8 \times 10^{19}$ (3×10^{20}) cm^{-3} along the *y*-direction. Thus, the high *ZT* values can be achieved at a practically relevant doping concentration. The combination of a large PF and low k_l leads to this impressive figure of merit, particularly along the *y*-direction for electron doping. The obtained *ZT* values are comparable to the typical anisotropic materials for the intermediate temperature range (500–900 K) as shown in Fig. 7(c); details of all the materials are listed in Table S3 of Supplemental Material [44] (see also Refs. [11,14,24,35,72–82]). Furthermore, the *ZT* value of β-$SrZrS_3$ is much higher than that for the commercially used material

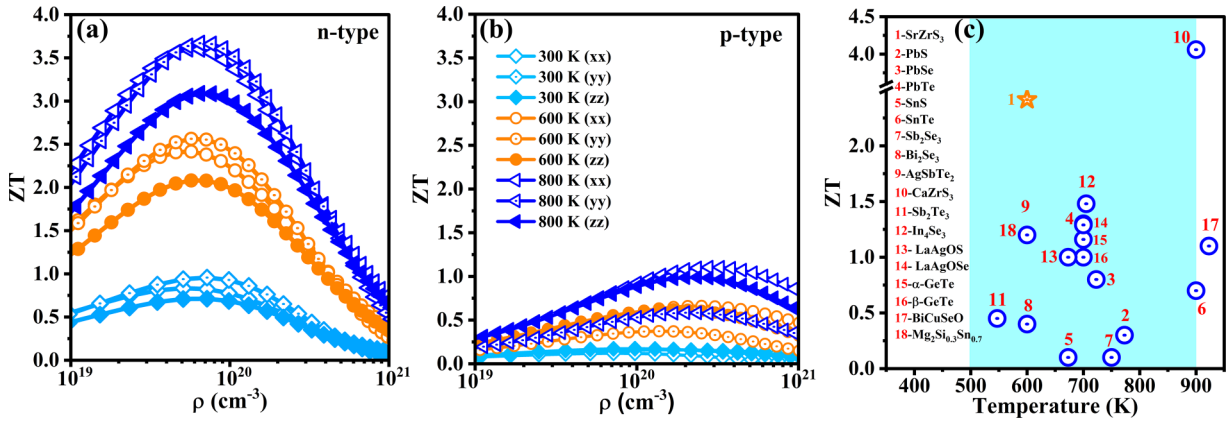

FIG. 7. [(a), (b)] The thermoelectric figure of merit ZT as a function of carrier concentration along the x-, y-, and z-axes at 300, 600, and 800 K for n-type and p-type doping, respectively. (c) A comparison between the ZT of reported intermediate-temperature TE material and β-$SrZrS_3$ tabulated in the Supplemental Material [44], Table S3 (see also Refs. [11,14,24,35,72–82]).

PbTe ($ZT < 1$), and the ZT values for single inorganic halide perovskites such as $CsSnI_3$, $CsGeI_3$, and $CsPbI_3$ are reported to be 0.95, 1.05, and 0.45 at 700 K, respectively [71]. Finally, it is suggested that the excellent TE performance of β-$SrZrS_3$ is made possible by controlling the electron concentration.

IV. CONCLUSION

In summary, the structural, electronic, and phonon transport properties of orthorhombic β-$SrZrS_3$ have been systematically investigated using DFT and transport calculations. A direct semiconducting nature with a band gap of 2.05 eV is noticed. The complex band structure with multiple valleys and band convergence in the conduction band is crucial for providing a significant power factor while n-type doping. The anisotropy is observed on the carrier effective mass and TE properties along all the axes. Phonon transport and lattice thermal conductivity are significantly impacted by the strong anharmonicity caused by the bond heterogeneity in the crystal structure. In particular, the weakly bound SrS_8 bicapped trigonal prisms are attributed to the noticed low average $\kappa_l \sim 1.26\,\mathrm{W\,m^{-1}\,K^{-1}}$ at 300 K and desirable ultralow average $\kappa_l \sim 0.64$ and $\sim 0.48\,\mathrm{W\,m^{-1}\,K^{-1}}$ at 600 and 800 K, respectively. Further, ADP, POP, and IMP scattering analysis near the band edge suggests that the POP dominance decides the overall mobility. Finally, based on the high Seebeck coefficient and low lattice thermal conductivity, the impressive ZT values, such as 3.67 for n-type and 1.10 for p-type at 800 K, are reported at doping concentrations 8×10^{19} and $3 \times 10^{20}\,\mathrm{cm^{-3}}$, respectively. This study on β-$SrZrS_3$ as a high ZT material may serve as a promising candidate for wide-band-gap-based TE devices.

ACKNOWLEDGMENTS

The authors acknowledge National Supercomputing Mission (NSM) for providing computing resources of "PARAM Smriti" at NABI, Mohali, which is implemented by C-DAC and supported by the Ministry of Electronics and Information Technology (MeitY) and Department of Science and Technology (DST), Government of India. S.R. acknowledges the DST Inspire JRF Fellowship (through Project No. IF190512).

[1] D. T. Crane and J. W. Lagrandeur, Progress report on BSST-led US Department of Energy automotive waste heat recovery program, J. Electron. Mater. **39**, 2142 (2010).
[2] D. Champier, Thermoelectric generators: A review of applications, Energy Convers. Manage. **140**, 167 (2017).
[3] D. Enescu and E. O. Virjoghe, A review on thermoelectric cooling parameters and performance, Renew. Sustain. Energy Rev. **38**, 903 (2014).
[4] W. He, G. Zhang, X. Zhang, J. Ji, G. Li, and X. Zhao, Recent development and application of thermoelectric generator and cooler, Appl. Energy **143**, 1 (2015).
[5] J. He and T. M. Tritt, Advances in thermoelectric materials research: Looking back and moving forward, Science **357**, 1369 (2017).
[6] A. E. Risseh, H. P. Nee, and C. Goupil, Electrical power conditioning system for thermoelectric waste heat recovery in commercial vehicles, IEEE Trans. Transp. Electr. **4**, 548 (2018).
[7] A. Witze, Nuclear power: Desperately seeking plutonium, Nature **515**, 484 (2014).
[8] B. Luo, D. Ye, and L. Wang, Recent progress on integrated energy conversion and storage systems, Adv. Sci. **4**, 1700104 (2017).
[9] C. Gayner and K. K. Kar, Recent advances in thermoelectric materials, Prog. Mater Sci. **83**, 330 (2016).
[10] D. Kraemer, B. Poudel, H. P. Feng, J. C. Caylor, B. Yu, X. Yan, Y. Ma, X. Wang, D. Wang, A. Muto, K. McEnaney, M. Chiesa, Z. Ren, and G. Chen, High-performance flat-panel solar thermoelectric generators with high thermal concentration, Nat. Mater. **10**, 532 (2011).
[11] L. D. Zhao, S. Hao, S. H. Lo, C. I. Wu, X. Zhou, Y. Lee, H. Li, K. Biswas, T. P. Hogan, C. Uher, C. Wolverton, V. P. Dravid, and M. G. Kanatzidis, High thermoelectric performance via hierarchical compositionally alloyed nanostructures, J. Am. Chem. Soc. **135**, 7364 (2013).

[12] Z. Li, H. Xie, Y. Xia, S. Hao, K. Pal, M. G. Kanatzidis, C. Wolverton, and X. Tang, Weak-bonding elements lead to high thermoelectric performance in $BaSnS_3$ and $SrSnS_3$: A first-principles study, Chem. Mater. **34**, 1289 (2022).

[13] T. Zhu, Y. Liu, C. Fu, J. P. Heremans, J. G. Snyder, and X. Zhao, Compromise and synergy in high-efficiency thermoelectric materials, Adv. Mater. **29**, 1605884 (2017).

[14] Y. Pei, H. Wang, and G. J. Snyder, Band engineering of thermoelectric materials, Adv. Mater. **24**, 6125 (2012).

[15] M. Jonson and G. D. Mahan, Mott's formula for the thermopower and the Wiedemann-Franz law, Phys. Rev. B **21**, 4223 (1980).

[16] T. Hendricks, T. Caillat, and T. Mori, Keynote review of latest advances in thermoelectric generation materials, devices, and technologies, Energies **15**, 7307 (2022).

[17] R. Chami, A. Lekdadri, L. H. Omari, E. K. Hlil, and M. Chafi, Investigation of the photovoltaic properties of $BaHf_{1-x}Zr_xS_3$ ($x \leqslant 1$) chalcogenide perovskites using first principles calculations, Mater. Today Energy **20**, 100689 (2021).

[18] A. Majumdar, Thermoelectricity in semiconductor nanostructures, Science **303**, 777 (2004).

[19] J. P. Heremans, V. Jovovic, E. S. Toberer, A. Saramat, K. Kurosaki, A. Charoenphakdee, S. Yamanaka, and G. J. Snyder, Enhancement of thermoelectric of the electronic density of states, Science **321**, 554 (2008).

[20] H. S. Kim, N. A. Heinz, Z. M. Gibbs, Y. Tang, S. D. Kang, and G. J. Snyder, High thermoelectric performance in $(Bi_{0.25}Sb_{0.75})_2Te_3$ due to band convergence and improved by carrier concentration control, Mater. Today **20**, 452 (2017).

[21] Y. Xiao and L. Zhao, Charge and phonon transport in PbTe-based thermoelectric materials, npj Quantum Mater. **3**, 55 (2018).

[22] P. Chen, H. Wu, B. Zhang, Z. Zhou, S. Zheng, L. Dai, Y. Huo, D. Zhang, Y. Yan, K. Peng, G. Han, X. Lu, X. Zhou, and G. Wang, Intrinsically low lattice thermal conductivity and anisotropic thermoelectric performance in in-doped $GeSb_2Te_4$ single crystals, Adv. Funct. Mater. **33**, 2211281 (2023).

[23] M. Wuttig, V. L. Deringer, X. Gonze, C. Bichara, and J. Raty, Incipient metals: Functional materials with a unique bonding mechanism, Adv. Mater. **30**, 1803777 (2018).

[24] Y. Yu, M. Cagnoni, O. Cojocaru-mirédin, and M. Wuttig, Chalcogenide thermoelectrics empowered by an unconventional bonding mechanism, Adv. Funct. Mater. **30**, 1904862 (2020).

[25] M. Tachibana, T. Kolodiazhnyi, and E. Takayama-Muromachi, Thermal conductivity of perovskite ferroelectrics, Appl. Phys. Lett. **93**, 092902 (2008).

[26] H. Muta, K. Kurosaki, and S. Yamanaka, Thermoelectric properties of reduced and La-doped single-crystalline SrTiO3, J. Alloys Compd. **392**, 306 (2005).

[27] T. Jia, Z. Feng, S. Guo, X. Zhang, and Y. Zhang, Screening promising thermoelectric materials in binary chalcogenides through high-throughput computations, ACS Appl. Mater. Interfaces **12**, 11852 (2020).

[28] D. Tiwari, O. S. Hutter, and G. Longo, Chalcogenide perovskites for photovoltaics: Current status and prospects, J. Phys. Energy **3**, 034010 (2021).

[29] J. Xi, W. Zhu, X. Li, D. Jiang, R. Dronskowski, and X. Shi, Discovery of high-performance thermoelectric chalcogenides through reliable high-throughput material screening, J. Am. Chem. Soc. **140**, 10785 (2018).

[30] K. V. Sopiha, C. Comparotto, J. A. Márquez, and J. J. S. Scragg, Chalcogenide perovskites: Tantalizing prospects, challenging materials, Adv. Opt. Mater. **10**, 2101704 (2022).

[31] S. J. Adjogri and E. L. Meyer, Chalcogenide Perovskites and perovskite-based chalcohalide as photoabsorbers: A study of their properties, and potential photovoltaic applications, Materials **14**, 7857 (2021).

[32] M. G. Ju, J. Dai, L. Ma, and X. C. Zeng, Perovskite chalcogenides with optimal bandgap and desired optical absorption for photovoltaic devices, Adv. Energy Mater. **7**, 1700216 (2017).

[33] Y. Y. Sun, M. L. Agiorgousis, P. Zhang, and S. Zhang, Chalcogenide perovskites for photovoltaics, Nano Lett. **15**, 581 (2015).

[34] S. Perera, H. Hui, C. Zhao, H. Xue, F. Sun, C. Deng, N. Gross, C. Milleville, X. Xu, D. F. Watson, B. Weinstein, Y. Y. Sun, S. Zhang, and H. Zeng, Chalcogenide perovskites - an emerging class of ionic semiconductors, Nano Energy **22**, 129 (2016).

[35] X. Song, X. Shai, S. Deng, J. Wang, J. Li, X. Ma, X. Li, T. Wei, W. Ren, L. Gao, Y. Fu, H. Wang, and C. Zeng, Anisotropic chalcogenide perovskite $CaZrS_3$: A promising thermoelectric material, J. Phys. Chem. C **126**, 11751 (2022).

[36] E. Osei-Agyemang, N. Koratkar, and G. Balasubramanian, Examining the electron transport in chalcogenide perovskite $BaZrS_3$, J. Mater. Chem. C **9**, 3892 (2021).

[37] H. Shahmohamadi and S. S. Naghavi, Sulfide perovskites for thermoelectricity, Appl. Mater. Interfaces **13**, 14189 (2021).

[38] S. Niu, J. Milam-Guerrero, Y. Zhou, K. Ye, B. Zhao, B. C. Melot, and J. Ravichandran, Thermal stability study of transition metal perovskite sulfides, J. Mater. Res. **33**, 4135 (2018).

[39] H. I. Eya, E. Ntsoenzok, and N. Y. Dzade, First–principles investigation of the structural, elastic, electronic, and optical properties of α– and β-$SrZrS_3$: Implications for photovoltaic applications henry, Materials **13**, 978 (2020).

[40] G. Kresse and J. Furthmüller, Efficient iterative schemes for ab initio total-energy calculations using a plane-wave basis set, Phys. Rev. B **54**, 11169 (1996).

[41] P. E. Blöchl, Projector augmented-wave method, Phys. Rev. B **50**, 17953 (1994).

[42] J. P. Perdew, K. Burke, and M. Ernzerhof, Generalized Gradient Approximation Made Simple, Phys. Rev. Lett. **77**, 3865 (1996).

[43] J. Heyd, G. E. Scuseria, and M. Ernzerhof, Erratum: Hybrid functionals based on a screened coulomb potential [J. Chem. Phys. **118**, 8207 (2003)], J. Chem. Phys. **124**, 2005(E) (2006).

[44] See Supplemental Material at http://link.aps.org/supplemental/10.1103/PhysRevMaterials.7.085403 for Bader charge analysis, Fermi surface, PBE, PBE+SOC band structure, mechanical properties, convergence test of phonon transport calculations, AMSET parameters, and comparison of ZT to reported materials.

[45] R. Nelson, C. Ertural, J. George, V. L. Deringer, G. Hautier, and R. Dronskowski, LOBSTER: Local orbital projections, atomic charges, and chemical-bonding analysis from projector-augmented-wave-based density-functional theory, J. Comput. Chem. **41**, 1931 (2020).

[46] A. Togo and I. Tanaka, First principles phonon calculations in materials science, Scr. Mater. **108**, 1 (2015).

[47] W. Li, J. Carrete, N. A. Katcho, and N. Mingo, ShengBTE: A solver of the boltzmann transport equation for phonons, Comput. Phys. Commun. **185**, 1747 (2014).
[48] G. Qin and M. Hu, Accelerating evaluation of converged lattice thermal conductivity, npj Comput. Mater. **4**, 3 (2018).
[49] S. Ju, T. Shiga, L. Feng, and J. Shiomi, Revisiting PbTe to identify how thermal conductivity is really limited, Phys. Rev. B **97**, 184305 (2018).
[50] A. M. Ganose, J. Park, A. Faghaninia, R. Woods-Robinson, K. A. Persson, and A. Jain, Efficient calculation of carrier scattering rates from first principles, Nat. Commun. **12**, 2222 (2021).
[51] G. K. H. Madsen, J. Carrete, and M. J. Verstraete, BoltzTraP$_2$, a program for interpolating band structures and calculating semi-classical transport coefficients, Comput. Phys. Commun. **231**, 140 (2018).
[52] C. Lee, K. M. Kleinke, and H. Kleinke, Synthesis, structure, and electronic and physical properties of the two $SrZrS_3$ modifications, Solid State Sci. **7**, 1049 (2005).
[53] K. Momma and F. Izumi, *VESTA 3* for three-dimensional visualization of crystal, volumetric and morphology data, J. Appl. Crystallogr. **44**, 1272 (2011).
[54] H. P. A. Savin, O. Jepsen, J. Flad, O. K. Andersen, and H. G. von Schnering, Electron localization in solid-state structures of the elements: The diamond structure, Angew. Chem. Int. Ed. **31**, 187 (1992).
[55] T. Tohei, A. Kuwabara, F. Oba, and I. Tanaka, Debye temperature and stiffness of carbon and boron nitride polymorphs from first principles calculations, Phys. Rev. B **73**, 064304 (2006).
[56] F. Mouhat and F. X. Coudert, Necessary and sufficient elastic stability conditions in various crystal systems, Phys. Rev. B **90**, 224104 (2014).
[57] P. Zhang, B. Chen, W. Zhu, C. Wang, W. Zhang, Y. Li, and W. Liu, First-principles prediction of structural, mechanical and thermal properties of perovskite $BaZrS_3$, Eur. Phys. J. B **93**, 97 (2020).
[58] R. T. Delves, Thermomagnetic effects in semiconductors and semimetals, Rep. Prog. Phys. **28**, 249 (1965).
[59] Y. Tang, Z. M. Gibbs, L. A. Agapito, G. Li, H. S. Kim, M. B. Nardelli, S. Curtarolo, and G. J. Snyder, Convergence of multi-valley bands as the electronic origin of high thermoelectric performance in $CoSb_3$ skutterudites, Nat. Mater. **14**, 1223 (2015).
[60] G. J. Wang, G. Heng, F. Ramya, C. Chenguang, Z. Runzi, and S. Tiejun, Thermoelectric transport effects beyond single parabolic band and acoustic phonon scattering, Mater. Adv. **3**, 734 (2022).
[61] K. Kuroki and R. Arita, "Pudding Mold" band drives large thermopower in Na_xCoO_2, J. Phys. Soc. Jpn. **76**, 083707 (2007).
[62] Y. Pei, X. Shi, A. Lalonde, H. Wang, L. Chen, and G. J. Snyder, Convergence of electronic bands for high performance bulk thermoelectrics, Nature (London) **473**, 66 (2011).
[63] W. G. Zeier, A. Zevalkink, Z. M. Gibbs, G. Hautier, M. G. Kanatzidis, and G. J. Snyder, Thinking like a chemist: Intuition in thermoelectric materials angewandte, Angew. Chem. Int. Ed. **55**, 6826 (2016).
[64] S. Niu, H. Huyan, Y. Liu, M. Yeung, K. Ye, L. Blankemeier, T. Orvis, D. Sarkar, D. J. Singh, R. Kapadia, and J. Ravichandran, Bandgap control via structural and chemical tuning of transition metal perovskite chalcogenides, Adv. Mater. **29**, 1604733 (2017).
[65] Y. Xiao, C. Chang, Y. Pei, D. Wu, K. Peng, X. Zhou, S. Gong, J. He, Y. Zhang, Z. Zeng, and L. D. Zhao, Origin of low thermal conductivity in SnSe, Phys. Rev. B **94**, 125203 (2016).
[66] E. Osei-Agyemang, C. E. Adu, and G. Balasubramanian, Ultralow lattice thermal conductivity of chalcogenide perovskite $CaZrSe_3$ contributes to high thermoelectric figure of merit, npj Comput. Mater. **5**, 116 (2019).
[67] Z. Zhang, K. Yuan, J. Zhu, X. Fan, J. Zhou, and D. Tang, Thermal conductivity of $SrTiO_3$ under high-pressure, Appl. Phys. Lett. **120**, 262201 (2022).
[68] G. A. Slack, Nonmetallic crystals with high thermal conductivity, J. Phys. Chem. Solids **34**, 321 (1973).
[69] J. Ma, Y. Chen, and W. Li, Intrinsic phonon-limited charge carrier mobilities in thermoelectric SnSe, Phys. Rev. B **97**, 205207 (2018).
[70] J. Cao, J. D. Querales-flores, A. R. Murphy, S. Fahy, and I. Savi, Dominant electron-phonon scattering mechanisms in *n*-type PbTe from first principles, Phys. Rev. B **98**, 205202 (2018).
[71] U.-G. Jong, Y.-S. Kim, C.-H. Ri, Y.-H. Kye, and C.-J. Yu, High thermoelectric performance in the cubic inorganic cesium iodide perovskites $CsBI_3$ (B = Pb, Sn, and Ge) from first-principles, J. Phys. Chem. C **125**, 6013 (2021).
[72] L. D. Zhao, J. He, C. I. Wu, T. P. Hogan, X. Zhou, C. Uher, V. P. Dravid, and M. G. Kanatzidis, Thermoelectrics with earth abundant elements: High performance p-Type PbS nanostructured with SrS and CaS, J. Am. Chem. Soc. **134**, 7902 (2012).
[73] W. He, D. Wang, J. F. Dong, Y. Qiu, L. Fu, Y. Feng, Y. Hao, G. Wang, J. Wang, C. Liu, J. F. Li, J. He, and L. D. Zhao, Remarkable electron and phonon band structures lead to a high thermoelectric performance: ZT >1 in earth-abundant and eco-friendly SnS crystals, J. Mater. Chem. A **6**, 10048 (2018).
[74] L. D. Zhao, X. Zhang, H. Wu, G. Tan, Y. Pei, Y. Xiao, C. Chang, D. Wu, H. Chi, L. Zheng, S. Gong, C. Uher, J. He, and M. G. Kanatzidis, Enhanced thermoelectric properties in the counter-doped SnTe system with strained endotaxial SrTe, J. Am. Chem. Soc. **138**, 2366 (2016).
[75] F. Jiang, C. Xia, Y. Zhu, Z. Han, C. Liu, J. Xia, Y. Chen, and W. Liu, Thermoelectric properties of p-type polycrystalline $Bi_{0.8}Sb_{0.8}In_{0.4}Se_3$, Appl. Phys. Lett. **118**, 4 (2021).
[76] B. L. Du, H. Li, and X. F. Tang, Enhanced thermoelectric performance in na-doped p-type nonstoichiometric $AgSbTe_2$ compound, J. Alloys Compd. **509**, 2039 (2011).
[77] L. P. Hu, T. J. Zhu, X. Q. Yue, X. H. Liu, Y. G. Wang, Z. J. Xu, and X. B. Zhao, Enhanced figure of merit in antimony telluride thermoelectric materials by in-ag co-alloying for mid-temperature power generation, Acta Mater. **85**, 270 (2015).
[78] X. Yin, J. Y. Liu, L. Chen, and L. M. Wu, High thermoelectric performance of In_4Se_3-based materials and the influencing factors, Acc. Chem. Res. **51**, 240 (2018).
[79] A. R. Natarajan, L. Ponvijayakanthan, M. K. Gupta, R. Mittal, and D. J. Singh, High thermoelectric performance of layered LaAgXO (X = Se, Te) from electrical and thermal transport calculations, Phys. Rev. Mater. **7**, 025405 (2023).
[80] S. Perumal, S. Roychowdhury, D. S. Negi, R. Datta, and K. Biswas, High thermoelectric performance and enhanced mechanical stability of P-Type $Ge_{1-x}Sb_xTe$, Chem. Mater. **27**, 7171 (2015).

[81] J. Sui, J. Li, J. He, Y. L. Pei, D. Berardan, H. Wu, N. Dragoe, W. Cai, and L. D. Zhao, Texturation boosts the thermoelectric performance of BiCuSeO oxyselenides, Energy Environ. Sci. **6**, 2916 (2013).

[82] G. K. Goyal, S. Mukherjee, R. C. Mallik, S. Vitta, I. Samajdar, and T. Dasgupta, High thermoelectric performance in $Mg_2(Si_{0.3}Sn_{0.7})$ by enhanced phonon scattering, ACS Appl. Energy Mater. **2**, 2129 (2019).